5-1-2012

Conformational and Thermodynamic Properties Modulate the Nucleotide Excision Repair of 2-Aminofluorene and 2-Acetylaminofluorene dG Adducts in the NarI Sequence

Vipin Jain
College of Pharmacy

Benjamin Hilton
East Tennessee State University

Satyakam Patnaik
College of Pharmacy

Yue Zou
East Tennessee State University

M. Paul Chiarelli
Loyola University of Chicago

See next page for additional authors

Follow this and additional works at: https://dc.etsu.edu/etsu-works

Citation Information

Conformational and Thermodynamic Properties Modulate the Nucleotide Excision Repair of 2-Aminofluorene and 2-Acetylaminofluorene dG Adducts in the NarI Sequence

Copyright Statement

Creative Commons License

Creator(s)

Vipin Jain, Benjamin Hilton, Satyakam Patnaik, Yue Zou, M. Paul Chiarelli, and Bongsup P. Cho

Conformational and thermodynamic properties modulate the nucleotide excision repair of 2-aminofluorene and 2-acetylaminofluorene dG adducts in the *NarI* sequence

Vipin Jain[1], Benjamin Hilton[2], Satyakam Patnaik[1], Yue Zou[2], M. Paul Chiarelli[3] and Bongsup P. Cho[1,*]

[1]Department of Biomedical and Pharmaceutical Sciences, University of Rhode Island, Kingston, RI 02881, [2]Department of Biochemistry and Molecular Biology, East Tennessee State University, Johnson City, TN 37614 and [3]Department of Chemistry, Loyola University, Chicago, IL 60626, USA

ABSTRACT

Nucleotide excision repair (NER) is a major repair pathway that recognizes and corrects various lesions in cellular DNA. We hypothesize that damage recognition is an initial step in NER that senses conformational anomalies in the DNA caused by lesions. We prepared three DNA duplexes containing the carcinogen adduct *N*-(2′-deoxyguanosin-8-yl)-7-fluoro-2-acetylaminofluorene (FAAF) at G_1, G_2 or G_3 of *NarI* sequence (5′-CCG$_1$G$_2$CG$_3$CC-3′). Our ^{19}F-NMR/ICD results showed that FAAF at G_1 and G_3 prefer syn S- and W-conformers, whereas anti B-conformer was predominant for G_2. We found that the repair of FAAF occurs in a conformation-specific manner, i.e. the highly S/W-conformeric G_3 and -G_1 duplexes incised more efficiently than the B-type G_2 duplex ($G_3\sim G_1 > G_2$). The melting and thermodynamic data indicate that the S- and W-conformers produce greater DNA distortion and thermodynamic destabilization. The *N*-deacetylated *N*-(2′-deoxyguanosin-8-yl)-7-fluoro-2-aminofluorene (FAF) adducts in the same *NarI* sequence are repaired 2- to 3-fold less than FAAF: however, the incision efficiency was in order of $G_2\sim G_1 > G_3$, a reverse trend of the FAAF case. We have envisioned the so-called *N*-acetyl factor as it could raise conformational barriers of FAAF versus FAF. The present results provide valuable conformational insight into the sequence-dependent UvrABC incisions of the bulky aminofluorene DNA adducts.

INTRODUCTION

Adduct formation is an important aspect of DNA damage: if unrepaired, various mutations in DNA could occur (1–3). The presence of mutations on specific onco-genes or tumor suppressor genes may trigger cancer initiation. Human cells are armed with various effective repair pathways to safeguard genomic DNA from continuous assault by exogenous and endogenous sources (4). Nucleotide excision repair (NER) is a major repair pathway that is known for the removal of stretches of bases containing various lesions, including single-base damages, bulky adducts and cross-links, among others (5). Deficiencies in NER are closely associated with the development of several genetic diseases, such as xeroderma pigmentosum that increases the risk of skin cancer due to higher sensitivity to sunlight (6).

The NER pathway in *Escherichia coli* involves the UvrABC nuclease system and has been studied extensively for understanding DNA damage recognition and incision. *E. coli* NER is initiated following damage recognition by a dimeric UvrA protein. Next, UvrB protein reaches the damage site, forms a trimer and verifies the damage. Departure of UvrA from the resulting complex recruits UvrC and UvrD proteins, which cleave and remove the lesion-bearing patch of DNA. Finally, DNA polymerase I synthesizes and ligase I seals a new patch to complete the repair process (5,7).

---

*To whom correspondence should be addressed. Tel: +1 401 874 5024; Fax: +1 401 874 5766; Email: bcho@uri.edu
Present address:
Department of Biomedical and Pharmaceutical Sciences, University of Rhode Island Fogarty Hall, 41 Lower College Road, Kingston, RI, 02881, USA

Arylamines are an important class of environmental pollutants that are implicated in the etiology of human cancers, especially of the bladder and liver (1). 2-Acetylaminofluorene was originally developed as an agricultural insecticide, but was later banned due to its strong tumorigenic activity in rat livers (8). It has been used extensively as a model for studying chemical carcinogenesis. *In vivo*, metabolic activation of AAF produces a highly electrophilic nitrenium ion, which subsequently interacts with DNA to produce two major C8-substituted dG adducts: AAF and AF (Figure 1a) (8,9). *In vitro*, *N*-acetylated AAF blocks the activity of high-fidelity polymerases and requires bypass polymerases for a translesion synthesis (TLS), whereas AF only slows down replication (10). In general, the bulky AAF exhibits greater susceptibility towards NER than AF (11), which is known to exist in a sequence-dependent equilibrium between *anti* B-conformer and *syn* S-conformer (Figure 1c) (10,12–14). We recently reported that AAF adducts also adopt a sequence-dependent S/B/W-conformational equilibrium (Figure 1d) (15).

Local sequence context plays an important role in the repair of arylamine–DNA adducts (16). Fuchs *et al.* constructed DNA sequences modified with AAF at each of three guanines of the most frequently studied mutational hotspot known as *Nar*I sequence ($5'-\ldots CG_1G_2CG_3$ $CC\ldots-3'$) and tested their substrate repairability in the *E. coli* UvrABC and human exonuclease systems. In *E. coli*, the three AAFs were repaired in a sequence-dependent manner, with relative repair efficiencies of $G_1:G_2:G_3$ in a ratio of 100:18:66 (17,18). However, different repair efficiencies were observed for the same lesions

by the human exonuclease, 38:100:68 for G_1, G_2 and G_3, respectively (18). AAF at G_3 of *Nar*I sequence induces ~100-fold greater frequency of −2 frameshift (−2 deletion) mutations, even though the three guanines exhibit similar chemical reactivities (19). We have shown that the FAF-modified *Nar*I -2 deletion duplex in the 5'–$CG_1G_2C\underline{G_3^*CC}$-3' context adopts a single looped-out bulge structure, whereas the 5'–$CG_1G_2C\underline{G_3^*CT}$–3' context results in a local conformational heterogeneity (20). These results support the importance of the 3'-next flanking nucleotide to the lesion in modulation of mutation efficiency. The studies verified that the conformational stability of a slipped mutagenic intermediate is a critical determinant for the hotness (up to 30- to 50-fold) of G_3 in *Nar*I sequence for −2 frameshift mutation (20–22). Mekhovich *et al.* (23) found a greater incision rate in *E. coli* systems when AAF was located at G_3 of the *Nar*I sequence (5'—$CG_1G_2CG_3^*CC$—3') than in a non-*Nar*I sequence (5'—GATG*ATA—3'). Zou *et al.* (24) have reported that the UvrABC incision efficiency is 70% more in the TG*T than in the CG*C sequence context when adducted with either AF- or AAF lesions.

The NER pathway is characterized by its unique ability to excise a wide array of structurally diverse DNA lesions. The structure of individual adducts *per se* is not as important as lesion-induced local distortions and destabilizations to trigger a NER response. Examples include disruption of Watson–Crick hydrogen bonding, DNA bending, thermodynamic destabilization, local conformational flexibility and flipped-out bases in the unmodified complementary strand (25,26). However, mechanisms of sequence dependence that control NER efficiencies remained elusive.
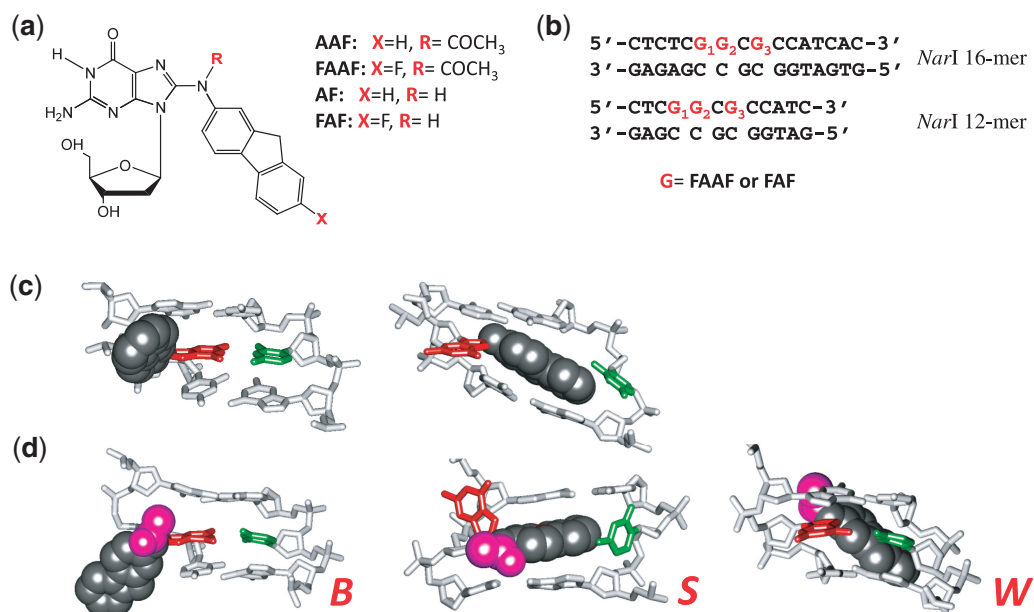
Figure 1. (**a**) Chemical structures of AAF, FAAF, AF and FAF adducts; (**b**) sequences of fully paired 16-mer and 12-mer *Nar*I duplexes used in the present study; major groove views of the central trimer segments of (**c**) the B/S and (**d**) B/S/W-conformer equilibrium of FAF and FAAF-modified duplexes. The modified dG and the complementary dC are shown in red and green sticks, respectively, and the aminofluorene moiety is highlighted with shiny gray CPK and the *N*-acetyl with pink CPK. In the B-type conformer, anti-[FAAF/FAF]dG maintains Watson–Crick hydrogen bonds, thereby placing the carcinogen moiety in the major groove. The carcinogens in the S- and W-conformers stack into the helix or wedged into the minor groove, respectively, with the modified dG in the syn conformation.

It could be that the observed local sequence effects described in the previous paragraph for AF and AAF are due to differences in the extent of distortions, which in turn depends on the conformation adopted in a particular sequence context.

In the present work, we investigated the role of conformational heterogeneity in the structure–repair relationships of AF and AAF. These two adducts are structurally similar, but differ in the absence and presence, respectively, of an *N*-acetyl group on the central nitrogen. We prepared oligonucleotides that were site-specifically modified by the fluorine model FAF and FAAF at three different guanines (G_1, G_2 and G_3) of the *Nar*I recognition sequences (Figure 1a and b). We conducted spectroscopic and melting experiments for conformational and thermodynamic analyses. Moreover, we performed NER studies of these adducts using the *E. coli* UvrABC system. The results present strong structural and thermodynamic evidences for the differential NER efficiencies exhibited by AF and AAF at different guanine residues of the *Nar*I sequence.

MATERIALS AND METHODS

Caution

2-Aminofluorene derivatives are mutagens and suspected human carcinogens and therefore must be handled with caution.

Crude oligodeoxynucleotides (ODN, 10 μmol scale) in desalted form were purchased from Eurofins MWG operon (Huntsville, AL, USA). All HPLC solvents were purchased from Fisher Inc. (Pittsburgh, PA, USA).

Preparation and characterization of FAF- and FAAF-modified ODNs

We previously reported the preparation of 12-mer *Nar*I ODNs (5′-CTCG$_1$G$_2$CG$_3$CCATC-3′), in which each of the three guanine were site-specifically modified by FAF (20). We have also demonstrated that the incorporation of

fluorine atom at the longest axis position 7 does not affect the overall conformational and thermal/thermodynamic profiles of AF- or AAF-modified duplexes (14,20). The three FAF-modified *Nar*I sequences were each annealed with a complementary 12-mer sequence (5′-GATGGCGC CGAG-3′) to form fully paired *Nar*I–G$_1$–FAF, *Nar*I–G$_2$–FAF and *Nar*I–G$_3$–FAF duplexes, respectively. These duplexes were thoroughly characterized by ^{19}F-NMR, CD and UV melting experiments (20).

FAAF-modified 16-mer ODN were prepared using the general procedures described previously (15,27). Briefly, approximately 0.5–1 mg of *N-acetoxy-N-2-(acetylamino)-7-fluorofluorene* dissolved in absolute ethanol was added drop wise to a sodium citrate buffer (pH 6.0) containing 200–250 ODs of unmodified ODN (5′-CTCTCG$_1$G$_2$CG$_3$CCATCAC-3′) and placed in a shaker for 5 min at 37°C. Figure 2a shows a typical reversed-phase HPLC chromatogram derived from the resulting mixture. The FAAF modified oligomers appearing between 28 and 85 min were separated and purified up to >97% purity by repeated injections. The HPLC system consisted of a Hitachi EZChrom Elite HPLC unit with an L2450 diode array detector and a Phenomenex Luna C18 column (150 × 10 mm, 5.0 μm). We employed a gradient system involving 3–15% acetonitrile for 40 min followed by 15–20% and 20–35% acetonitrile for 20 and 40 min, respectively, in pH 7.0 ammonium acetate buffer (100 mM) with a flow rate of 2.0 ml/min.

The three FAAF-modified 16-mer sequences were each annealed with the complementary sequence (5′-GTGATG GCGCCGAGAG-3′) to form fully paired *Nar*I–G$_1$–FAAF, *Nar*I–G$_2$–FAAF and *Nar*I–G$_3$–FAAF duplexes for UV melting, DSC, CD and dynamic ^{19}F-NMR experiments.

LC/MS characterization of FAAF-modified ODNs

Electrospray ionization and quadrupole time-of-flight mass spectrometry was utilized to verify the molecular weights and the position of FAAF attachment of the
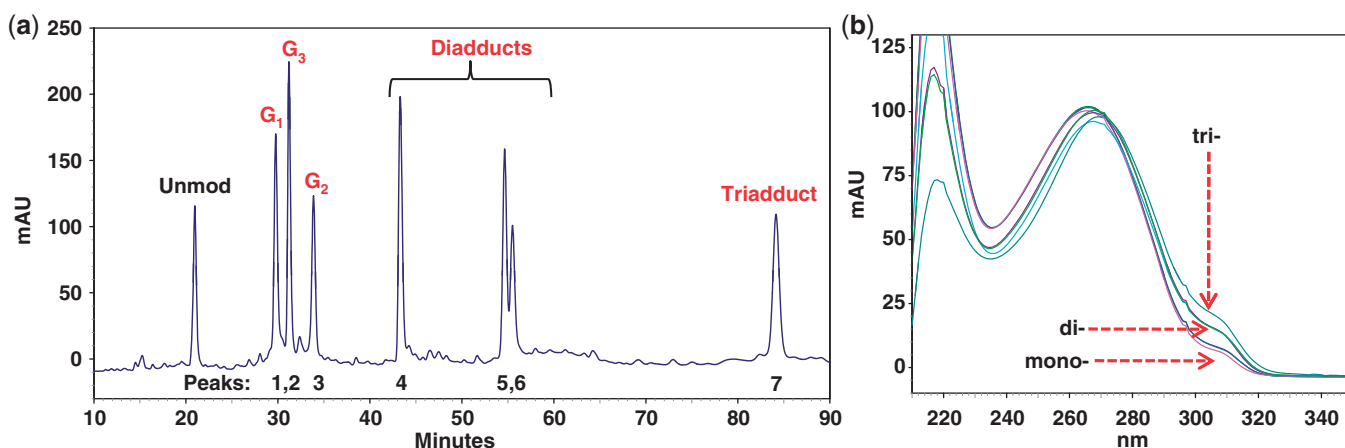
Figure 2. (a) Chromatogram of a reaction mixture between 16-mer *Nar*I sequence (5′-CTCTCG$_1$G$_2$CG$_3$CCATCAC-3′) and an activated FAAF (*N*-acetoxy-*N*-2-(acetylamino)-7-fluorofluorene). The mono- (G$_1$, G$_3$, G$_2$), di- and tri-FAAF adducts eluted in the 28–35, 42–60 and 84 min were purified by reversed-phase HPLC (see 'Materials and Methods' section for gradient condition); (b) online photodiode array UV/Vis spectra of mono-, di- and tri-FAAF adducts.

three oligomers. The 16-mer ODNs were sequenced using 3′–5′ or 5′–3′ exonucleases as described previously for the analysis of modified 12-mers (28). Normally, 1 µg of a particular ODN was combined with 0.01 units of an exonuclease in a 1 mM solution of $MgCl_2$ and incubated for several hours. The digests were separated using a Phenomenex Aqua C18, 1.0×50 mm column (5 µm; 120 Å). Solvent A was 5 mM in both ammonium acetate and dimethylbutyl amine. Acetic acid was added to solvent A to adjust the pH to 7.0. Solvent B was 0.1% formic acid in acetonitrile. The flow rate was 100 µl/min and total run time was 20 min. All LC/MS spectra were acquired using a Waters SYNAPT quadrupole time-of-flight mass spectrometer (Milford, MA, USA) operated in the negative ion and V-modes. The measured molecular masses of all three isomeric ODNs were within 0.1 Da of their theoretical monoisotopic mass (5016.9 Da).

UV melting

UV melting data were obtained using a Cary100 Bio UV/VIS spectrophotometer equipped with a 6×6 multi-cell block and 1.0 cm path length. Sample cell temperatures were controlled by an in-built Peltier temperature controller. Oligonucleotide duplexes with a concentration range of 0.4–6.4 µM were prepared in solutions containing 0.2 M NaCl, 10 mM sodium phosphate and 0.2 mM EDTA at pH 7.0. Thermomelting curves were constructed by varying temperature of the sample cell (1°C/min) and monitoring absorbance at 260 nm. A typical melting experiment consisted of forward/reverse scans and was repeated five times. Thermodynamic parameters were calculated using the program MELTWIN version 3.5 as described previously (12).

Circular dichroism

Circular dichroism (CD) measurements were conducted on a Jasco J-810 spectropolarimeter equipped with a Peltier temperature controller. Typically, 2 ODs of each strand were annealed with an equimolar amount of a complementary sequence. The samples were dissolved in 400 µl of a neutral buffer (0.2 M NaCl, 10 mM sodium phosphate, 0.2 mM EDTA) and placed in a 1.0 mm path length cell. The samples were heated at 85°C for 5 min and then cooled to 15°C, over a 10 min period to ensure complete duplex formation. Spectra were acquired every 0.2 nm with a 2 s response time from 200 to 400 nm at a rate of 50 nm/min, were the averages of 10 accumulations and were smoothed using 17-point adaptive smoothing algorithms provided by Jasco.

Dynamic ^{19}F-NMR

Approximately 20 ODs of a pure FAAF-modified 16-mer ODN was annealed with an equimolar amount of a complementary sequence to produce a fully paired duplex (Figure 1b). The samples were then dissolved in 300 µl of typical pH 7.0 NMR buffer containing 10% D_2O/90% H_2O, 100 mM NaCl, 10 mM sodium phosphate and 100 µM EDTA, and filtered into a Shigemi tube through a 0.2 µm membrane filter. All ^{1}H- and ^{19}F-NMR results were recorded using a dedicated 5 mm ^{19}F/^{1}H dual probe

on a Bruker DPX400 Avance spectrometer operating at 400.0 and 376.5 MHz, respectively, using acquisition parameters described previously (14, 20, 29). Imino proton spectra at 5°C were obtained using a phase-sensitive jump-return sequence and referenced relative to that of DSS. ^{19}F-NMR spectra were acquired in the ^{1}H-decoupled mode and referenced relative to that of $CFCl_3$ by assigning external C_6F_6 in C_6D_6 at −164.9 ppm. One and two-dimensional ^{19}F-NMR spectra were measured between 5 and 60°C with increment of 5–10°C. Temperatures were maintained by a Bruker-VT unit with the aid of controlled boiling liquid N_2 in the probe. Line shape simulations were performed as described previously (30) using WINDNMR-Pro (version 7.1.6; *J. Chem. Educ.* Software Series; Reich, H. J., University of Wisconsin, Madison, WI, USA).

DSC experiments

Calorimetric measurements of the three FAAF-modified 16-mer duplexes were performed using a Nano-DSC from TA Instruments (Lindon, UT, USA). Prior to temperature scanning, samples were degassed for at least 10 min under house vacuum in a closed vessel. Solutions were loaded, respectively, into the sample and reference cells using a pipette by attaching a small piece of silicone tube at the end of the tip and were purged several times to get rid of air bubbles. After both cells were filled, they were capped and a slight external pressure (~3 atm) was applied to prevent evaporation of the sample solution. Raw data were collected as microwatts versus temperature. Template–primer solutions were prepared by dissolving desalted samples in a pH 7.0 buffer solution consisting of 20 mM sodium phosphate and 0.1 M NaCl. In a typical scan, a 0.1 mM template–primer solution was scanned against buffer from 15°C to 90°C at a rate of 0.75°C/min. At least five repetitions were obtained. A buffer *vs.* buffer scan was used as a control and subtracted from the sample scan and normalized for heating rate. This results in base-corrected ΔC_p^{ex} versus temperature curves. Each transition shows negligible changes in the heat capacities between the initial and final states, thus $\Delta\Delta C_p^{ex}$ was assumed to be zero. The area of the resulting curve is proportional to the transition heat, which, when normalized for the number of moles of the sample, is equal to the transition enthalpy, ΔH. ΔH is an integration of ΔC_p^{ex} over temperature T. All sample solutions were 0.1 mM concentration. T_m was the temperature at half the peak area. ΔG and ΔS values have been determined according to the procedures described by Chakrabarti *et al.* (31).

Substrate construction and UvrABC protein purification

DNA substrates of 55 bp containing a FAAF adduct at each of three guanine residues were constructed as previously described (11,32). Briefly, an FAAF-modified 16-mer ODN (5′-CTCTCG$_1$G$_2$CG$_3$CCATCAC-3′) was ligated with flanking 20-mer ODN (5′-GACTACGTACT GTTACGGCT-3′) and 19-mer ODN (5′-GCAATCAGG CCAGATCTGC-3′) ODN at the 5′- and 3′-end, respectively (Supplementary Figure S1). The 20-mer was

5′-terminally labeled with ^{32}P. The ligation product was purified by urea–PAGE under denaturing conditions. Following the purification, the substrate was annealed to the corresponding complementary strand, and then purified on an 8% native polyacrylamide gel. Similar procedures were employed to construct FAF-modified DNA substrates using 12-mer *Nar*I sequence (5′-CTCG$_1$G$_2$CG$_3$CCATC-3′), which we prepared previously for ^{19}F-NMR/UV/ICD studies (20).

UvrA, UvrB and UvrC proteins were over expressed in *E. coli* and then purified as previously described (33). The estimated purity of the three proteins was >95%. A Bio-Rad Protein Assay was used to determine the protein concentration with BSA as the standard based on the manufacturer-recommended procedures.

Nucleotide excision assay and quantification of incision products

The 5′-terminally labeled DNA substrates were incised by UvrABC as previously described (11,32). Briefly, the DNA substrates (2 nM) were incubated in the UvrABC reaction buffer (50 mM Tris–HCl, pH 7.5, 50 mM KCl, 10 mM MgCl$_2$, 5 mM DTT) at 37°C in the presence of UvrABC (UvrA, 10 nM; UvrB, 250 nM; and UvrC, 100 nM). The Uvr proteins were diluted and premixed in Uvr storage buffer before addition to the reaction. Aliquots were collected at 0, 5, 10, 15 and 20 min into the reaction. The reaction was terminated by heating at 95°C for 5 min. The products were denatured by addition of formamide loading buffer and heating to 95°C for 5 min, followed by quick chilling on ice. The incision products were then analyzed by electrophoresis on a 12% polyacrylamide sequencing gel under denaturing conditions with TBE buffer.

To quantify the incision products, radioactivity was measured using a Fuji FLA-5000 Image Scanner with MultiGauge V3.0 software. The DNA incised (in fmol) by UvrABC was calculated based on the total molar amount of DNA used in each reaction and the ratio of the radioactivity of incision products to total radioactivity of DNA. At least three independent experiments were performed for determination of the rates of incision.

RESULTS

Model sequences

We previously used FAF-modified 12-mer duplexes (5′-CTCG$_1$G$_2$CG$_3$*C*NATC-3′, N = C or T) to probe the impact of flanking and 3′-next flanking sequences on *Nar*I-induced frameshift mutagenesis (20). Initially, we tried to use the same 12-mer *Nar*I sequence for FAAF-modification for sake of comparison and consistency; however, the sequence was unsuitable for FAAF. Although FAAF adduction on the 12-mer *Nar*I sequence was facile, a resulting reaction mixture was difficult to purify on the reverse phase HPLC system (see asterisked peaks in Supplementary Figure S2). Moreover, ligation efficiencies of the FAAF-modified 12-mers, particularly on the G$_1$- and G$_2$-positions, were very low. Accordingly, the length of DNA was increased

to 16 (5′-CTCTCGGCGCCATCAC-3′, Figure 1b) by adding two nucleotides (underlined) on either side of the 12-mer. The resulting FAAF-modified 16-mer ODNs were separated well on a reverse-phase HPLC and exhibited excellent ligation efficiencies (see below).

Figure 2a shows an HPLC profile of a work-up mixture after 20 min of reaction. Unreacted control ODN appeared at 21 min, followed by seven FAAF-modified ODNs in three retention time zones: Peaks 1–3 at 28–35 min, Peaks 4–6 at 42–60 min and Peak 7 at 84 min. Online UV (Figure 2b) of the modified ODNs displayed a small shoulder in the 290–320 nm range. The relative absorption intensities (290–320 nm) for the three peak groups were approximately 1:2:3. This finding is reminiscent of AF- or FAF-induced absorption shoulders observed in 290–350 nm, whose intensities correlate consistently with the number of adduct modifications (28). As a result, Peaks 1–3 and 4–6 were assigned as mono- and di-adducts, respectively, and Peak 7 as a tri-adduct. These adducts were characterized by exonuclease digestion/ESI-TOF-MS-MS analyses, as described below. Depending on the location of FAAF, the mono-adducts were designated as *Nar*I–G$_1$, *Nar*I–G$_2$ or *Nar*I–G$_3$, in which G$_1$, G$_2$ and G$_3$ signify the position of the FAAF-modified guanine. Details of the structural characterization and repair of the di- and tri-FAAF adducts will be published separately.

The HPLC elution profile of the FAAF-modified 16-mer ODNs in the present study is similar to that of the AAF-modified 15-mer *Nar*I sequence (5′-TCCTCG$_1$G$_2$CG$_3$CCTCTC-3′) reported by Tan *et al.* (34). These results indicate that AAF and FAAF are chromatographically comparable, irrespective of sequence length, as long as the common *Nar*I core (underlined) is included in the sequences. This is not surprising since conformational and thermodynamic compatibilities of fluorine containing AF and AAF models have well been documented (20,30,35). A similar elution pattern was observed for the FAF-modified 12-mer and FAAF-modified 16-mer *Nar*I sequences; however, the order of elution of G$_1$ and G$_3$ was reversed (compare Figure 2a with Figure 2 in Ref. 20).

ESI-QTOF-MS characterization

The molecular weights of all three FAAF-modified ODNs were measured by ESI-QTOF-MS prior to sequence verification by exonuclease digestion. Ionization of ODNs normally occurs by the loss of a proton from a phosphate group in the ODN backbone. As the number of nucleotides in an ODN increases, the average charge state observed in the full scan mass spectra increases as well (28). As shown in Supplementary Figure S3, the ODNs containing 16 nucleotides form $(M-4H)^{4-}$ ions predominantly unlike the 12-mers studied previously that form $(M-3H)^{3-}$ primarily upon electrospray (28). Exonucleases cleave terminal deoxynucleotides from the ODN chain until the FAAF-modified nucleotide is exposed at the end of the chain. At that point the digestion reaction slows down significantly. The position of modification is identified (in this case) when the fragment(s) formed by

the loss of the unmodified guanine nucleotides is observed in the LC/MS spectra. This is shown in Supplementary Figure S4 for the 3′ digest of the -G$_1$(FAAF)G$_2$CG$_3$-ODN. The ions observed at m/z 659.5 and m/z 989.7 are the (M-3 H)$^{3-}$ and (M-2 H)$^{2-}$ ions formed from the 5′-CT CTCG$_1$(FAAF)-3′ ODN digest fragment. The observation of these ions confirms that this ODN is modified on the G closest to the 5′ end. The LC/MS analysis of the 5′ digest of the second modified ODN to elute is shown in Supplementary Figure S5a and 5b. The exonuclease digestion of this particular reaction product was particularly slow and evidence for endonuclease activity is observed in the mass spectra. All the Y fragments observed in Supplementary Figure S5 are (M-3 H)$^{3-}$ ions. The Y10 and Y9 fragments at m/z 1069.2 (5′-G$_2$CG$_3$(FAAF)CCA TCAC-3′) and m/z 959.5 (5′-CG$_3$(FAAF)CCATCAC-3′) are formed by consecutive cleavages of unmodified guanines, confirming that this reaction product is modified on the guanine closest to the 3′ end. LC/MS analysis of the exonuclease digests derived from the third singly-modified ODN to elute indicates that the FAAF group is attached to the central G in the sequence, -G$_1$G$_2$(FAAF)CG$_3$-. LC/MS analysis of the 3′ digest (Supplementary Figure S6) show ions at m/z 1154.7 and m/z 769.5 corresponding to the (M-2 H)$^{2-}$ and (M-3 H)$^{3-}$ ions derived from the 5′-CTCTCG$_1$G$_2$(FAAF)-3′ digest fragment. The mass spectra acquired from the 5′-digest (Supplementary Figure S7) show (M-2 H)$^{2-}$ and (M-3 H)$^{3-}$ ions at m/z 1604.3 and m/z 1069.2 whose masses are consistent with 5′-G$_2$(FAAF)CG$_3$CCATCAC-3′ fragment. No ions formed by the loss of two guanine deoxynucleotides were observed in any of the mass spectra. The observation of ODN fragments with two G's in both 3′ and 5′ digests confirms that the last singly modified ODN to elute from the reaction mixture is modified on the middle G.

Circular dichroism

Figure 3a shows an overlay of the CD spectra for the three FAAF-modified *Nar*I–G$_1$, –G$_2$ and –G$_3$ duplexes relative to the unmodified control (red). Unmodified and FAAF-adducted duplexes both displayed a positive and negative ellipticity at around 270 and 250 nm, respectively, which is an S-curve characteristic of a B-form DNA double helix. The modified duplexes displayed significant blue shifts relative to the unmodified duplex, *Nar*I–G$_3$ (6 nm) >> *Nar*I–G$_1$ ∼ G$_2$ (3 nm), indicating adduct-induced DNA bending. A concomitant increase in the positive intensity around 270 nm was noted in the order of G$_3$ ∼ G$_1$ > G$_2$, which could be due to the interaction of the intercalated S-conformeric FAAF with neighboring bases. We noted a similar blue shift and hyperchromic effect for the highly (75%) S-conformeric FAF-modified *Nar*I–G$_3$ duplex (Figure 3b and Table 1 in Ref. 20).

More importantly, FAAF-modified duplexes exhibited sequence-dependent induced CD in the 290–320 nm range (ICD$_{290-320 nm}$). This finding is reminiscent of ICD$_{290-350 nm}$, which has been used as a sensitive marker for the FAF-induced S/B/W-conformational heterogeneity (positive for S- and W- and negative for B-conformer) (12, 15, 20, 29, 36). In the present case, however, the FAAF-modified *Nar*I duplexes exhibited negative dips, with the *Nar*I–G$_2$ duplex showing a greater dip than G$_1$ or G$_3$ duplexes (Figure 3a). This result could be due to a higher ratio (57%) of B-conformer for the *Nar*I–G$_2$ duplex.

UV melting experiments

Supplementary Figure S8 shows the UV melting profiles of the three FAAF–*Nar*I duplexes and an unmodified control duplex, all at 6.4 µM. All duplexes showed typical monophasic, sigmoidal, helix–coil transitions with a strong linear correlation ($R^2 > 0.9$) between T_m^{-1} and $\ln C_t$. Thermal and thermodynamic parameters calculated from UV melting are summarized in Supplementary Table S1. As expected, modified duplexes were destabilized thermally and thermodynamically relative to the control duplex. The magnitude of thermal (ΔT_m) and thermodynamic ($\Delta\Delta G$) destabilization was in the order of *Nar*I–G$_2$ ∼ *Nar*I–G$_3$ (−8.7 to −8.8°C, 3.3 to 3.7 kcal/mol, respectively) > *Nar*I–G$_1$ (−4.6°C and 2.0 kcal/mol, respectively).

Differential scanning calorimetry

Figure 3b shows differential scanning calorimetry (DSC) plots of excess heat capacity C_p^{ex} versus temperature for the FAAF–*Nar*I duplexes relative to the unmodified
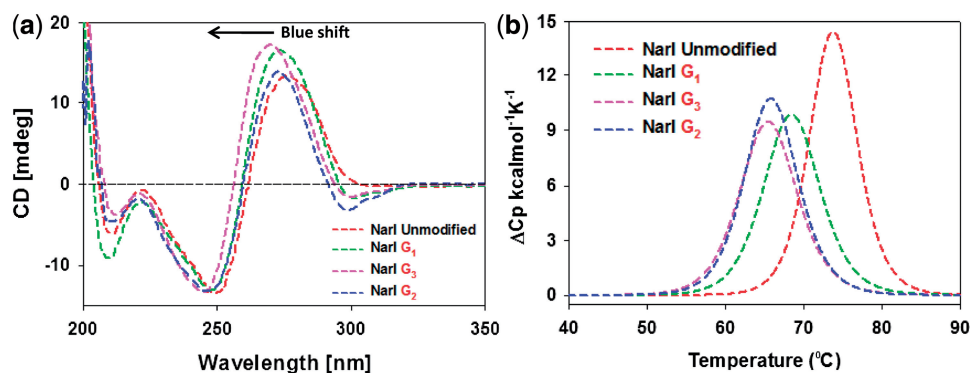

Figure 3. (a) CD spectral overlays recorded at 15°C and (b) DSC curves recorded in 20 mM phosphate buffer containing 0.1 M NaCl at pH 7.0 of fully paired 16-mer *Nar*I duplexes with FAAF modification at G$_1$ (green), G$_2$ (blue) and G$_3$ (pink).

Table 1. Thermal and thermodynamic parameters of FAAF modified *Nar*I duplexes obtained from differential scanning calorimetry

				5′-CTCTCG$_1$G$_2$CG$_3$CCATCAC-3′ 3′-GAGAGC C GCGGTAGTG-5′				
	$-\Delta H$ (kcal/mol)	$-\Delta S$ (eu)	$-\Delta G_{37°c}$ (kcal/mol)	T_m[a] (°C)	$\Delta\Delta H$[b] (kcal/mol)	$\Delta\Delta S$[c] (eu)	$\Delta\Delta G_{37°c}$[d] (kcal/mol)	ΔT_m[e] (°C)
Control[f]	117.5	319.1	18.6	73.9	–	–	–	–
*Nar*I-G$_1$-FAAF[f]	95.6	260.2	14.9	68.6	21.9	58.9	3.7	−5.3
*Nar*I-G$_2$-FAAF[f]	98.9	272.1	14.5	66.0	18.6	47.0	4.1	−7.9
*Nar*I-G$_3$-FAAF[f]	92.8	254.4	13.9	65.6	24.7	64.7	4.7	−8.3

[a]T_m values is the temperature at half the peak area.
[b]$\Delta\Delta H = \Delta H$ (modified duplex) $-\Delta H$ (control duplex).
[c]$\Delta\Delta S = \Delta S$ (modified duplex) $-\Delta S$ (control duplex).
[d]$\Delta\Delta G = \Delta G$ (modified duplex) $-\Delta G$ (control duplex).
[e]$\Delta T_m = T_m$ (modified duplex) $-T_m$ (control duplex).
[f]The average standard deviations for $-\Delta G$, $-\Delta H$ and T_m are ± 0.4, ± 3.0 and ± 0.4, respectively.

Table 2. Conformational heterogeneity (B/S/W), thermal destabilization and relative percent incision rates of FAAF- and FAF-modified *Nar*I duplexes

*Nar*I Duplexes	Population Ratios[a] (%)			ΔT_m[b] (°C)	Relative incision rate[c] (%)
	B	S	W		
*Nar*I-G$_1$-FAAF	46	34	20	−5.3	93
*Nar*I-G$_2$-FAAF	57	15	9	−7.9	32
*Nar*I-G$_3$-FAAF	13	61	26	−8.3	100
*Nar*I-G$_1$-FAF	42	58	–	−9.4	44
*Nar*I-G$_2$-FAF	69	31	–	−6.8	43
*Nar*I-G$_3$-FAF	35	65	–	−8.3	25

[a]The percent population ratios were calculated at 5°C on the basis of line simulations.
[b]$\Delta T_m = T_m$ (modified duplex) $- T_m$ (control duplex).
[c]Percent incision rate of modified duplexes with respect to *Nar*I-G$_3$-FAAF (100%).

control. Table 1 summarizes the thermal and thermodynamic parameters derived from these DSC curves. Consistent with the UV melting data, the *Nar*I–G$_3$ duplex was most destabilized ($\Delta\Delta H = 24.7$ kcal/mol, $\Delta\Delta G_{37°C} = 4.7$ kcal/mol, $\Delta T_m = -8.3°C$), followed by *Nar*I–G$_2$ ($\Delta\Delta G_{37°C} = 4.1$ kcal/mol, $\Delta T_m = -7.9°C$). *Nar*I–G$_1$ was the least affected ($\Delta\Delta G_{37°C} = 3.7$ kcal/mol, $\Delta T_m = -5.3°C$).

Differences in the thermal and thermodynamic destabilizations must have arisen from the differences in the S/B/W-conformational characteristics. The most S-conformeric (61%) *Nar*I–G$_3$ duplex causes disturbance of Watson–Crick base pairing, resulting in enthalpy reduction ($\Delta\Delta H = 24.7$ kcal/mol) (Table 2). However, the large entropy ($\Delta\Delta S = 64.7$ eu) compensates for the enthalpy, thus resulting in the overall free energy loss of $\Delta\Delta G_{37°C} = 4.7$ kcal/mol (37). In contrast, *Nar*I–G$_1$ and –G$_2$ duplexes possess higher populations of B-conformer (46 and 57%, respectively), thus exhibiting lower differences in the enthalpy values ($\Delta\Delta H = 21.9$ kcal/mol and $\Delta\Delta H = 18.6$ kcal/mol, respectively) (Table 2). The relatively small enthalpy differences observed for the G$_1$ and G$_2$ duplexes could be attributed to the presence of S- and

W-conformers in addition to B-conformer. As expected, entropy compensation was less in these two duplexes (*Nar*I–G$_1$, $\Delta\Delta S = 58.9$ eu and *Nar*I–G$_2$, $\Delta\Delta S = 47.0$ eu), yielding similar overall free energies (*Nar*I–G$_1$, $\Delta\Delta G = 3.7$ kcal/mol and *Nar*I–G$_2$, $\Delta\Delta G = 4.1$ kcal/mol).

S/B/W conformational heterogeneity

Figure 4a shows the ^{19}F-NMR spectra of FAAF–*Nar*I 16-mer G$_1$-, G$_2$- and G$_3$-duplexes measured at 5°C, in which ^{19}F signals are in slow chemical exchange. These *Nar*I-FAAF duplexes exhibited three to five ^{19}F signals, each representing a particular conformation. The percent population ratios shown were calculated on the basis of line simulations as shown in Supplementary Figure S9. Assignments of the different ^{19}F signals of each duplex were necessary to carry out meaningful structure-activity-relationship studies. The signal assignments in Figure 4a were made initially on the basis of chemical exchange, ring current effect and chemical shift pattern recognition as have been done for a number of FAAF- and FAF-adducts in various sequence contexts (30,35). It has been demonstrated that AF and AAF adducts adopt the S/B- and S/B/W-conformational equilibrium, respectively (Figure 1c and d) and their ^{19}F chemical shifts are independent of overall sequence and its length, but strongly rely on the nature of the bases flanking the lesion (15,30). The major ^{19}F signals in Figure 4a correlate well with the S/B/W-profiles reported previously for FAAF adducts (15), i.e. B-, S- and W-conformers going from downfield to upfield, i.e. −115.0 to −115.5, −115.5 to −117.0 and −117.0 to −118.0 ppm, respectively. Additional signals were observed in the −114.0∼−115.0 ppm range for the *Nar*I–G$_2$ and –G$_3$ duplexes (Figure 4a, see Supplementary Table S2 for exact chemical shifts). Consistent with this observation, their proton spectra displayed a mixture of broad imino signals arising not only from those involved in Watson–Crick hydrogen bonds (12–14 ppm), but also from the lesion site and its vicinity (11–12 ppm) (Supplementary Figure S10).

To complement the ^{19}F signal assignments, we additionally conducted a set of comparative spectral analyses using
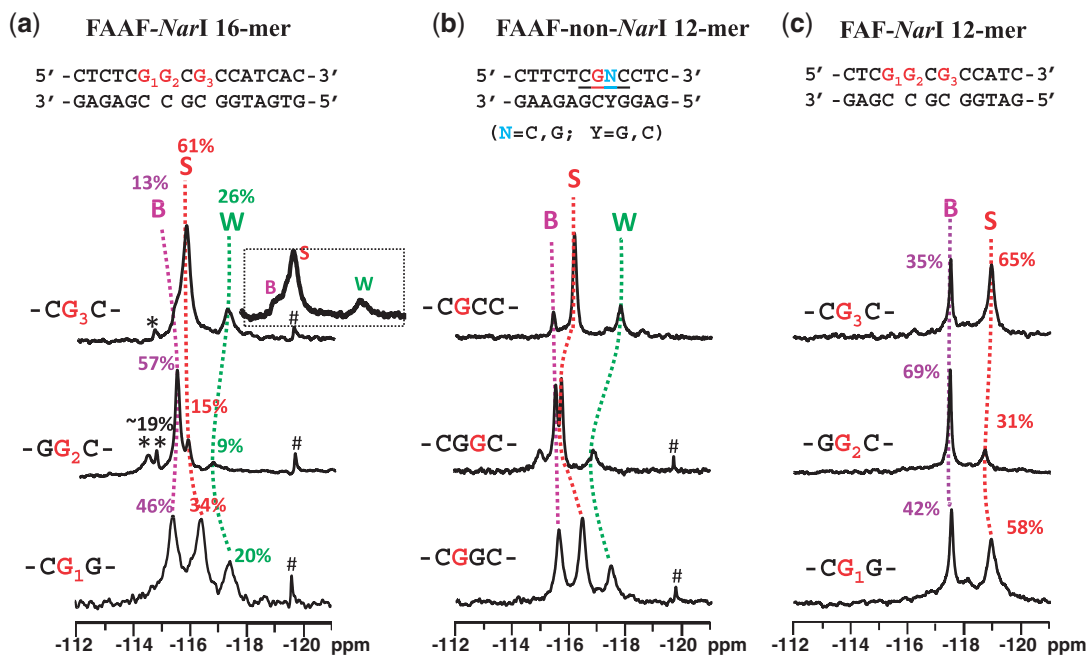
Figure 4. ^{19}F-NMR spectra of (**a**) FAAF-modified *Nar*I 16-mer, (**b**) FAAF-modified non-*Nar*I 12-mer and (**c**) FAF-modified *Nar*I 12-mer duplexes at 5°C. *unknown conformers; $^{\#}$impurity.

three FAAF-12-mer duplexes in the non-*Nar*I sequences (Figure 4b) in otherwise identical flanking sequence contexts (CG*G, GG*C and CG*C context for G_1, G_2 and G_3, respectively). The top trace in Figure 4b is the ^{19}F-NMR spectrum of a FAAF-modified 12-mer duplex (5'-CTTCT CG*CCCTC-3'), whose S/B/W conformational profiles have been well characterized (15). It should be noted that this non-*Nar*I 12-mer duplex contains the identical CG*C flanking sequence context as the 16-mer *Nar*I–G_3–FAAF duplex. Comparison of the two spectra (i.e. top traces of Figure 4a and b) revealed a parallel trend both in terms of chemical shifts and population ratios (Table 2 and Supplementary Table S2), supporting the conformational assignments. This is consistent with our previous findings that the electronic environment for the ^{19}F signals of AF and AAF adducts are strongly modulated by the nature of flanking bases (15, 30). Similarly, we prepared two additional FAAF-modified non-*Nar*I 12-mer duplexes (5'-CTTCT CG*GCCTC-3' and 5'-CTTCTC GG*CCTC-3') with the same flanking base contexts (underlined) as the *Nar*I–G_1 and –G_2 duplexes, respectively. Figure 4a and b compares the ^{19}F-NMR spectra of all three *Nar*I 16-mer and non-*Nar*I 12-mer duplexes side by side. The ^{19}F signal profiles, as indicated by dotted lines (pink, B; red, S; green, W) for $G_1 \rightarrow G_2 \rightarrow G_3$ of each sequence context, match quite well overall despite of slight variations observed in chemical shifts and population ratios, particularly for the GG*C sequence context. Whereas the S- and W-conformer signals were prone to shift, the B-conformer signal appeared to be steady at -115.5 ppm. This trend is more apparent in Supplemental Figure S11, in which the two FAAF-modified sequence series (*Nar*I-16-mer versus non-*Nar*I-12-mer) are compared in a pair for each –CG*G-, -GG*C- and

–CG*C- sequence contexts. It is plausible that the carcinogen moiety in the major groove of the B-conformer is not subjected to the ring current effect, as the S- and W-conformers would be (14). We were unable to identify the minor signals (asterisked) in the 16-mer *Nar*I–G_2– (<19%) and –G_3–FAAF duplexes, although their downfield shifts relative to the B-conformer imply B-like conformers, in which the fluorine containing carcinogen moiety is exposed.

Figure 4c shows the ^{19}F-NMR spectra of FAF-modified 12-mer duplexes with the same *Nar*I sequence contexts, which have been thoroughly characterized (20). The B/S conformer population ratios were determined to be 42%:58%, 69%:31%, 35%:65% for FAF-modified *Nar*I–G_1, –G_2 and –G_3, respectively, at 5°C (Table 2) (20). Although the chemical shift difference (0.4–1.0 ppm) for the B and S conformer of FAAF (Figure 4a) is significantly smaller than that ($\sim$1.5 ppm) of the FAF counterparts, their overall S/B ratios appear to match (Figure 4a and c). The B/S/W population ratios for the FAAF–*Nar*I–G_1, –G_2 and –G_3 16-mer duplexes were 46:34:20, 57:15:9 and 13:61:26, respectively (Table 2). In both the FAAF- (Figure 4a) and FAF- (Figure 4c) *Nar*I duplexes, the population of S-conformer decreased in the order of $G_3 > G_1 > G_2$ and that of the B-conformer decreased in the reverse order, $G_2 > G_1 > G_3$. This comparative analysis was based on the assumption that structurally similar FAAF would experience similar sequence effects on their conformational profiles as observed by FAF in different sequence contexts of the *Nar*I sequence (20). As expected, the aminofluorene-induced B/S-heterogeneity is strongly dependent on the nature of the flanking sequences, regardless of whether the lesion has the bulky acetyl group on the central
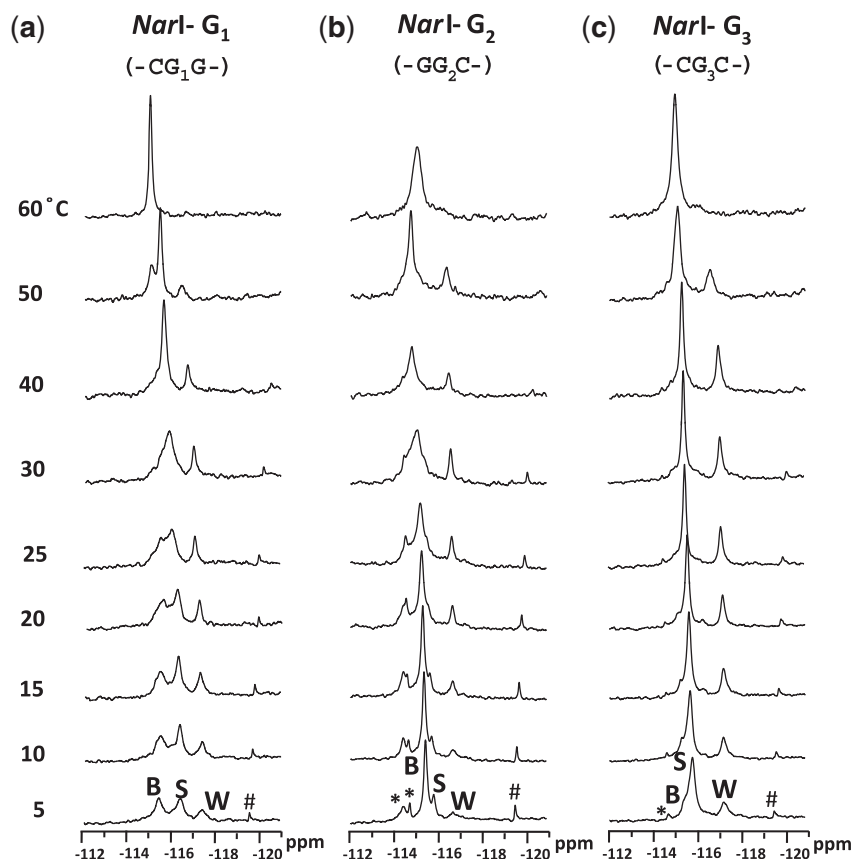
Figure 5. Dynamic ^{19}F-NMR spectra of fully paired 16-mer *Nar*I duplexes. FAAF modification at (**a**) G_1, (**b**) G_2 and (**c**) G_3. *unknown conformers; #impurity.

nitrogen linking the carcinogen and the modified guanine, thus validating our assumption.

Dynamic ^{19}F-NMR

Figure 5 shows the ^{19}F-NMR spectra of the three FAAF–*Nar*I duplexes as a function of temperature (5–60°C). Whereas the three ^{19}F signals in each duplex were in slow exchange at 5°C, the two downfield B- and S-signals became exchange broadened, giving rise to coalescent signals at around 30, 40 and 25°C for G_1, G_2 and G_3, respectively. In all cases, the merged signals coalesced with the upfield W-signal at around 60°C. All three *Nar*I duplexes showed relatively strong off-diagonal contour peaks of the major signals in the exchange spectra (data not shown), confirming their chemical exchanges.

UvrABC incisions of FAAF-adducts on *Nar*I sequence

Figure 6 shows the kinetic assay results, in which 55-mer FAAF-modified DNA duplex substrates were incised by UvrABC nuclease. These substrates were radioactively labeled at the 5′-end of the adducted strand. The major incision products can be seen as 18-mer (*Nar*I–G_1), 19-mer (*Nar*I–G_2) or 21-mer (*Nar*I–G_3) separated on a urea–PAGE gel under denaturing conditions (Supplementary Figure S12). The incision occurred at the eighth phosphate bond 5′ to the modified nucleotide, which is consistent

with the previously reported results of UvrABC incision (11,32).

Quantitative analysis of the incision indicated that the substrates were incised at different efficiencies, depending on where the damage site was located in the sequence (Figure 6). Specifically, the *N*-acetylated FAAF adducts at *Nar*I–G_1 and *Nar*I–G_3 displayed similar rates of incision, whereas *Nar*I–G_2 had a much lower rate of incision, G_3 (100%) $\geq G_1$ (93%) > G_2 (32%) (Figure 6c, Table 2). For comparison, we also determined the UvrABC incision of FAF adducts in the same *Nar*I sequence context. As shown in Figure 6b and c, the *N*-deacetylated FAF adducts in the same *Nar*I sequence context were repaired 2- to 3-fold less than FAAF. Despite having similar B/S-conformer profiles (Figure 4 and Table 2) the incision efficiency of FAF adducts at the three different sites in the *Nar*I sequence followed the order of G_1 (44%) $\approx G_2$ (43%) > G_3 (25%), where the percentages were calculated relative to FAAF *Nar*I–G_3 (which was the most efficiently incised).

DISCUSSION

It is well known that DNA sequence is a major determining factor for repair outcomes of site-specifically modified bulky DNA lesions. In this study, we examined the conformational heterogeneity and thermodynamics of
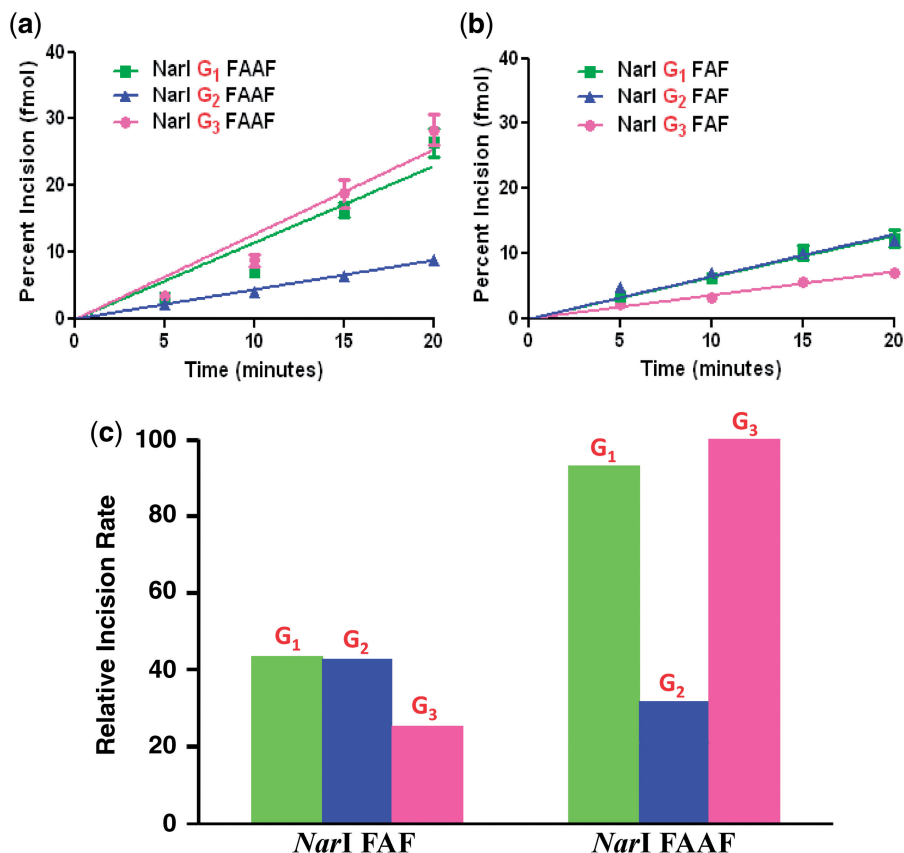
Figure 6. Absolute percent incision rates of (**a**) FAAF and (**b**) FAF–*Nar*I duplexes modified at G_1, G_2 and G_3; (**c**) percent incision rates histogram of FAF and FAAF at different positions relative to *Nar*I–G_3 FAAF as 100%.

FAAF and FAF at three different guanine positions (G_1, G_2 and G_3) of the well-known *Nar*I recognition sequence. Moreover, we obtained NER data of these adducts using the *E. coli* UvrABC system. Table 2, which summarizes the S/B/W solution conformational heterogeneity, T_m and NER efficiency results, presents strong evidence that the NER repair efficiencies of AAF and AF adducts in the *Nar*I sequences are modulated by their conformational and thermodynamic properties.

FAAF-induced B/S/W-conformational heterogeneity

Our combined ^{19}F-NMR/ICD results show that FAAF adduct in a well-known mutational hotspot *Nar*I sequence exist in a mixture of B/S/W conformers with varying populations (Figure 4a, Table 2). A greater population of *syn*-glycosidic S-(61%) and W-(26%) conformers was observed in *Nar*I–G_3, in which the lesion is flanked with C on both 5′- and 3′-ends (-CG$_3$*C-). This result is consistent with the preferred *syn*-conformation adopted by duplexes modified by AF (20), 2-amino-3-methylimidazo(4,5-*f*)quinolone (IQ) (38–40) and 2-amino-1-methyl-6-phenylimid-azo(4,5-*b*)pyridine (PHIP) (41), with the same -CG*C- contexts, in either *Nar*I or non-*Nar*I sequences (20,38,39,41). The mostly *syn Nar*I–G_3 duplex appeared to be distorted, bent or possibly formed a B–Z junction, as evidenced by a significant blue shift and hyperchromic effect in CD (Figure 3a) (42). The latter was probably due to the π–π stacking

interaction between the intercalated aminofluorene and flanking base pairs. On the other hand, the *Nar*I–G_2 duplex (-G$_1$G$_2$*C-) exhibited largely the *anti*-B-conformer (57%) along with S- (15%), W- (9%) and two unidentified minor conformers ($\sim$19%). In comparison to *Nar*I–G_3, the *Nar*I–G_2 duplex exhibited smaller blue shift and hyperchromic effect (Figure 3a), suggesting lesser disturbance of the double helical DNA structure.

These results indicate the heterogeneous nature of AAF in the *Nar*I sequence and are consistent with a previous CD study that showed a major DNA distortion for AAF at G_3 adduct compared to G_1 and G_2 (42). Similarly, Veaute *et al.* (43) conducted a DNase I footprint study on the *Nar*I sequence and showed that AAF at the G_2 position inhibits DNase I digestion of DNA at up to five bases in the modified strand and four bases in the complementary strand. In contrast, inhibition at the G_1 and G_3 positions was extended to eight and six bases, respectively in the modified strand.

The G_3 and G_2 duplexes are chemically isomeric, differing only in the direction of the G:C base pair at the 5′-position (e.g. C:G $\rightarrow$ G:C). Such a polarity swap is clearly responsible for the rather dramatic conformational shift from S- (61 to 15%) to B- (13 to 57%) and W-conformation (26 to 9%) (Table 2). A similar polarity switch at the 3′-end of the *Nar*I–G_1 duplex resulted in varying degrees of conformational shift in S- (61 to 34%), B- (13 to 46%) and W-conformation (26 to 20%).

As expected, FAAF-modification at the three guanines of the 16-mer *Nar*I sequence resulted in thermal (ΔT_m = −5.3 to −8.3°C) and thermodynamic ($\Delta\Delta G_{37°C}$ = 3.7–4.7 kcal/mol) destabilization relative to the unmodified control duplex (Table 1). The destabilizing effect of the FAAF modification was sequence-dependent and was related to the S/B/W-conformational profile. As summarized in Tables 1 and 2, the highly S-conformeric *Nar*I–G_3 duplex (61%) promoted lesion stacking and disrupted the lesion site Watson–Crick base pairs, resulting in thermal (ΔT_m = −8.3°C) and enthalpic destabilization ($\Delta\Delta H$ = 24.7 kcal/mol). In contrast, the highly B-conformeric (57%) *Nar*I–G_2 duplex exerted less enthalpy change ($\Delta\Delta H$ = 18.6 kcal/mol). As expected, *Nar*I–G_1 (46% B, 34% S) produced an intermediate change in enthalpy ($\Delta\Delta H$ = 21.9 kcal/mol). In all cases, however, enthalpy–entropy compensation resulted in a small overall difference (∼1 kcal/mol) in thermodynamic destabilization (Table 1). A similar case could occur if the W-conformer was considered as a thermodynamic destabilizer, G_3 (26%) > G_1 (20%) > G_2 (9%). We previously studied three fully paired FAF-modified 12-mer duplexes in the same *Nar*I sequence contexts (20). The UV melting results showed that FAF modification destabilizes the duplexes (ΔT_m = −6.8 to −9.4°C, $\Delta\Delta G$ = 4.2–4.6 kcal/mol) similarly. The highly S-conformeric (65%) *Nar*I–G_3 duplex resulted in thermal destabilization (ΔT_m = −8.3°C), whereas the highly B-conformeric (69%) *Nar*I–G_2 duplex exerted less destabilization (ΔT_m = −6.8°C) (Table 2) (20).

Conformation-specific nucleotide excision repair

The *E. coli* UvrABC system displayed significant differences in repair of the FAAF adduct at each guanine position (G_1, G_2 and G_3) of the *Nar*I sequence. The *Nar*I–G_2 duplex showed considerably lower efficiency than *Nar*I–G_1 or *Nar*I–G_3, [G_3 (100%) ≥ G_1 (93%) > G_2 (32%)] (Figure 6). It is clear from Table 2 that these NER results are in good agreement with the order of the S-conformer population [G_3 (61%) > G_1 (34%) > G_2 (15%)], but are in exactly the reverse order of the population of B-conformer, [G_2 (57%) > G_1 (46%) > G_3 (13%)]. This data suggest that the S-conformation is recognized and incised by *E. coli* NER dominantly over the B-conformation. We reported previously a similar conformation-specific NER results on a series of FAF-modified duplexes (16, 30).

The carcinogen in the highly S-conformer *Nar*I–G_3 is base-displaced at the lesion site, thus resulting in a major disturbance in the DNA helical structure (ΔT_m = −8.3°C, $\Delta\Delta G_{37°C}$ = 4.7 kcal/mol) (Table 2). This finding is contrasted with the 57% B-conformer *Nar*I–G_2 duplex, which maintains Watson–Crick base pairs at the lesion site (ΔT_m = −7.9°C, $\Delta\Delta G_{37°C}$ = 4.1 kcal/mol). Similar correlations could be made with either the W-conformer alone, G_3 (26%) > G_1 (20%) > G_2 (9%) or the *syn*-conformation (combined S and W), G_3 (87%) > G_1 (54%) > G_2 (24%).

For comparison, we also determined the UvrABC incisions of FAF-adducts in the same *Nar*I sequence context.

The two lesions revealed a similar B/S conformer heterogeneity in the *Nar*I sequence context (Figure 4). Therefore, the expectation was that FAF would show a similar NER profile as FAAF, i.e. S-/W-conformer promotes NER over B-conformer. However, the NER results revealed that incision efficiency was in the order of $G_1 \approx G_2 > G_3$ (Figure 6, Table 2). At first, this result appears to be in line with the B-conformer population. It should be noted that FAF is repaired consistently 2- to 3-fold less than FAAF (Figure 6c, Table 2). This result is a general trend reported in the literature, although much greater differences in incision efficiency between AF and AAF have been noted (11, 44). As a result, the difference between G_1 and G_2 of FAF is not statistically significant (P = 0.83), but their difference with G_3 is significant ($P < 0.0001$).

The incision differences between FAAF and FAF seem to suggest that, in addition to the sequence-dependent adduct conformation, the acetyl group in FAAF may play a role in DNA damage recognition by UvrABC. The only structural difference between FAF and FAAF is the absence of a bulky acetyl group on the linking nitrogen of the former (Figure 1a). It has been documented that *N*-acetylated FAAF adducts in fully paired duplexes produce a mixture of complex S/B/W-conformers, whereas *N*-deacetylated FAF adopts a simple exchangeable S/B-equilibrium (15, 30). Thus, it is clear that the *N*-acetyl group is responsible for generating up to 26% W-conformer in the *Nar*I sequence (Figure 4). The bulkiness of the acetyl group with its possibility for *cis* and *trans* rotamer transitions about the amide bond (14, 15, 45) may facilitate the repositioning of the fluorenyl rings into the minor groove from the S conformation. This conformational rearrangement is relatively straightforward since it does not require a change in the glycosidic bond, which is *syn* in both cases. We observed a good correlation between the proportion of W-conformation and NER efficiency of FAAF.

Moreover, although FAF and FAAF have similar S/B-conformational profile (Figure 4), the *N*-acetyl group in the latter could act as a 'conformational locker' to raise the energy barriers among conformers. Such a scenario, i.e. higher energy barriers of FAAF *vs.* FAF, is plausible and might contribute to a greater disturbance in DNA, and thus greater repair. By contrast, the *N*-deacetylated FAF adopts a facile interchangeable B/S-equilibrium (<2 kcal/mol) that triggers weaker binding affinities with the damage-recognition protein UvrA. A recent crystal study indicated that the UvrA dimer does not contact the lesion site directly, but rather binds DNA regions on both sides of the modification and primarily recognizes adduct-induced unwinding, bending and deformity in the overall DNA structure (25). Furthermore, DNA damage recognition in *E. coli* NER is achieved through a sequential 2-step mechanism (46). The initial step is to recognize the adduct-induced distorted DNA structure. After strand opening at the damage site, the DNA adduct structure is further recognized or verified in a second step, which may facilitate the flipping of the adducted nucleotide (47,48). Therefore, it is possible that, for FAF, the second step of recognition plays a more

important role than the first step, whereas the first step is a dominate recognition for FAAF.

The order of NER efficiencies described here is roughly consistent with bacterial NER data on AAF adducts embedded in a similar *Nar*I sequence (17): G_1 (100%), G_3 (66%) and G_2 (18%). Sequence dependence was also found in human NER of AAF adducted in the *Nar*I sequence (18). In contrast to the *E. coli* NER data, however, the AAF adduct at G_2 (100%) was found to be more repairable, followed by G_3 (68%) and G_1 (38%). Despite differences in the nature of proteins involved in prokaryotic and eukaryotic NER, the two systems show similar involvement of β-hairpin intrusion as damage recognition factors (49). Liu *et al.* (50) found a general qualitative trend toward similar relative NER incision efficiencies for 65% of bulky benzo[a]pyrene and equine estrogen substrates. Similar to bacterial UvrA, Rad4 (XPC) in yeast also recognizes helical distortion to sense DNA damage; unlike bacteria, yeast use a base-flipping mechanism for repair (26). Therefore, the efficiency of repair depends not only on the damage recognition step, but also on other factors, such as ease of base flipping.

In summary, our structural and thermodynamic data provide valuable conformational insights into the sequence-dependent UvrABC incisions of the bulky FAF and FAAF adducts in the *Nar*I sequence context. Repair of the bulky *N*-acetylated FAAF adduct seems to occur in a conformation-specific manner, i.e. the highly S/W-conformeric G_3 and G_1 duplexes incised considerably more efficiently than the G_2 duplex ($G_3 \sim G_1 > G_2$) (Table 2). These results were supported by melting and thermodynamic data. Not surprisingly, FAF was repaired 2- to 3-fold less than FAAF; however, the order of incision efficiencies was the reverse of that in the FAAF case. We considered the so-called *N*-acetyl factor and lesion-specific recognition mechanism for the different orders of incision for FAF and FAAF. Finally, the temperature dependence of the S/B/W-conformational equilibria of the FAAF-adducts in the *Nar*I sequence could provide valuable opportunities for conformation-specific NER utilizing thermophilic UvrABC proteins (51). Taken together, the results of this study demonstrate the complexity of NER mechanisms of bulky DNA lesions.

SUPPLEMENTARY DATA

Supplementary Data are available at NAR Online: Supplementary Tables S1–S2, Supplementary Figures S1–S12.

FUNDING

Conflict of interest statement. None declared.

REFERENCES

1. Luch,A. (2005) Nature and nurture - lessons from chemical carcinogenesis. *Nat. Rev. Cancer*, **5**, 113–125.
2. Melchior,W.B. Jr, Marques,M.M. and Beland,F.A. (1994) Mutations induced by aromatic amine DNA adducts in pBR322. *Carcinogenesis*, **15**, 889–899.
3. Neumann,H.G. (2007) Aromatic amines in experimental cancer research: tissue-specific effects, an old problem and new solutions. *Crit. Rev. Toxicol.*, **37**, 211–236.
4. Friedberg,E.C., Walker,G.C., Siede,W., Wood,R.D., Schultz,R.A. and Ellenberger,T. (eds), (2006) *DNA Repair and Mutagenesis*, 2nd edn. ASM Press, Washington.
5. Truglio,J.J., Croteau,D.L., Van Houten,B. and Kisker,C. (2006) Prokaryotic nucleotide excision repair: the UvrABC system. *Chem. Rev.*, **106**, 233–252.
6. Lehmann,A.R. (2003) DNA repair-deficient diseases, xeroderma pigmentosum, Cockayne syndrome and trichothiodystrophy. *Biochimie*, **85**, 1101–1111.
7. Van Houten,B. (1990) Nucleotide excision repair in Escherichia coli. *Microbiol. Rev.*, **54**, 18–51.
8. Heflich,R.H. and Neft,R.E. (1994) Genetic toxicity of 2-acetylaminofluorene, 2-aminofluorene and some of their metabolites and model metabolites. *Mutat. Res.*, **318**, 73–114.
9. Beland,F.A. and Kadlubar,F.F. (1990) *Handbook of Experimental Pharmacology*. Spring, Heidelberg.
10. Cho,B.P. (2004) Dynamic conformational heterogeneities of carcinogen-DNA adducts and their mutagenic relevance. *J. Environ. Sci. Health C. Environ. Carcinog. Ecotoxicol. Rev.*, **22**, 57–90.
11. Luo,C., Krishnasamy,R., Basu,A.K. and Zou,Y. (2000) Recognition and incision of site-specifically modified C8 guanine adducts formed by 2-aminofluorene, N-acetyl-2-aminofluorene and 1-nitropyrene by UvrABC nuclease. *Nucleic Acids Res.*, **28**, 3719–3724.
12. Meneni,S.R., D'Mello,R., Norigian,G., Baker,G., Gao,L., Chiarelli,M.P. and Cho,B.P. (2006) Sequence effects of aminofluorene-modified DNA duplexes: thermodynamic and circular dichroism properties. *Nucleic Acids Res.*, **34**, 755–763.
13. Patel,D.J., Mao,B., Gu,Z., Hingerty,B.E., Gorin,A., Basu,A.K. and Broyde,S. (1998) Nuclear magnetic resonance solution structures of covalent aromatic amine-DNA adducts and their mutagenic relevance. *Chem. Res. Toxicol.*, **11**, 391–407.
14. Zhou,L., Rajabzadeh,M., Traficante,D.D. and Cho,B.P. (1997) Conformational heterogeneity of arylamine-modified DNA: 19F NMR evidence. *J. Am. Chem. Soc.*, **119**, 5384–5389.
15. Patnaik,S. and Cho,B.P. (2010) Structures of 2-acetylaminofluorene modified DNA revisited: insight into conformational heterogeneity. *Chem. Res. Toxicol.*, **23**, 1650–1652.
16. Meneni,S., Shell,S.M., Zou,Y. and Cho,B.P. (2007) Conformation-specific recognition of carcinogen-DNA adduct in Escherichia coli nucleotide excision repair. *Chem. Res. Toxicol.*, **20**, 6–10.
17. Seeberg,E. and Fuchs,R.P. (1990) Acetylaminofluorene bound to different guanines of the sequence -GGCGCC- is excised with different efficiencies by the UvrABC excision nuclease in a pattern not correlated to the potency of mutation induction. *Proc. Natl Acad. Sci. USA*, **87**, 191–194.
18. Mu,D., Bertrand-Burggraf,E., Huang,J.C., Fuchs,R.P., Sancar,A. and Fuchs,B.P. (1994) Human and E.coli excinucleases are affected differently by the sequence context of acetylaminofluorene-guanine adduct. *Nucleic Acids Res.*, **22**, 4869–4871.
19. Burnouf,D., Koehl,P. and Fuchs,R.P. (1989) Single adduct mutagenesis: strong effect of the position of a single acetylaminofluorene adduct within a mutation hot spot. *Proc. Natl Acad. Sci. USA*, **86**, 4147–4151.
20. Jain,N., Li,Y., Zhang,L., Meneni,S.R. and Cho,B.P. (2007) Probing the sequence effects on *Nar*I-induced -2 frameshift mutagenesis by dynamic 19F NMR, UV, and CD spectroscopy. *Biochemistry*, **46**, 13310–13321.

21. Broschard,T.H., Koffel-Schwartz,N. and Fuchs,R.P. (1999) Sequence-dependent modulation of frameshift mutagenesis at *Nar*I-derived mutation hot spots. *J. Mol. Biol.*, **288**, 191–199.

22. Koffel-Schwartz,N. and Fuchs,R.P. (1995) Sequence determinants for -2 frameshift mutagenesis at *Nar*I-derived hot spots. *J. Mol. Biol.*, **252**, 507–513.

23. Mekhovich,O., Tang,M. and Romano,L.J. (1998) Rate of incision of N-acetyl-2-aminofluorene and N-2-aminofluorene adducts by UvrABC nuclease is adduct- and sequence-specific: comparison of the rates of UvrABC nuclease incision and protein-DNA complex formation. *Biochemistry*, **37**, 571–579.

24. Zou,Y., Shell,S.M., Utzat,C.D., Luo,C., Yang,Z., Geacintov,N.E. and Basu,A.K. (2003) Effects of DNA adduct structure and sequence context on strand opening of repair intermediates and incision by UvrABC nuclease. *Biochemistry*, **42**, 12654–12661.

25. Jaciuk,M., Nowak,E., Skowronek,K., Tanska,A. and Nowotny,M. (2011) Structure of UvrA nucleotide excision repair protein in complex with modified DNA. *Nat. Struct. Mol. Biol.*, **18**, 191–197.

26. Min,J.H. and Pavletich,N.P. (2007) Recognition of DNA damage by the Rad4 nucleotide excision repair protein. *Nature*, **449**, 570–575.

27. Cho,B.P. and Zhou,L. (1999) Probing the conformational heterogeneity of the acetylaminofluorene-modified 2'-deoxyguanosine and DNA by 19F NMR spectroscopy. *Biochemistry*, **38**, 7572–7583.

28. Gao,L., Zhang,L., Cho,B.P. and Chiarelli,M.P. (2008) Sequence verification of oligonucleotides containing multiple arylamine modifications by enzymatic digestion and liquid chromatography mass spectrometry (LC/MS). *J. Am. Soc. Mass Spectrom.*, **19**, 1147–1155.

29. Jain,N., Meneni,S., Jain,V. and Cho,B.P. (2009) Influence of flanking sequence context on the conformational flexibility of aminofluorene-modified dG adduct in dA mismatch DNA duplexes. *Nucleic Acids Res.*, **37**, 1628–1637.

30. Meneni,S.R., Shell,S.M., Gao,L., Jurecka,P., Lee,W., Sponer,J., Zou,Y., Chiarelli,M.P. and Cho,B.P. (2007) Spectroscopic and theoretical insights into sequence effects of aminofluorene-induced conformational heterogeneity and nucleotide excision repair. *Biochemistry*, **46**, 11263–11278.

31. Chakrabarti,M.C. and Schwarz,F.P. (1999) Thermal stability of PNA/DNA and DNA/DNA duplexes by differential scanning calorimetry. *Nucleic Acids Res.*, **27**, 4801–4806.

32. Zou,Y., Liu,T.M., Geacintov,N.E. and Van Houten,B. (1995) Interaction of the UvrABC nuclease system with a DNA duplex containing a single stereoisomer of dG-(+)- or dG-(-)-anti-BPDE. *Biochemistry*, **34**, 13582–13593.

33. Zou,Y. and Van Houten,B. (1999) Strand opening by the UvrA(2)B complex allows dynamic recognition of DNA damage. *EMBO J.*, **18**, 4889–4901.

34. Tan,X., Suzuki,N., Grollman,A.P. and Shibutani,S. (2002) Mutagenic events in Escherichia coli and mammalian cells generated in response to acetylaminofluorene-derived DNA adducts positioned in the Nar I restriction enzyme site. *Biochemistry*, **41**, 14255–14262.

35. Meneni,S., Liang,F. and Cho,B.P. (2007) Examination of the long-range effects of aminofluorene-induced conformational heterogeneity and its relevance to the mechanism of translesional DNA synthesis. *J. Mol. Biol.*, **366**, 1387–1400.

36. Liang,F., Meneni,S. and Cho,B.P. (2006) Induced circular dichroism characteristics as conformational probes for carcinogenic aminofluorene-DNA adducts. *Chem. Res. Toxicol.*, **19**, 1040–1043.

37. Liang,F. and Cho,B.P. (2010) Enthalpy-entropy contribution to carcinogen-induced DNA conformational heterogeneity. *Biochemistry*, **49**, 259–266.

38. Elmquist,C.E., Wang,F., Stover,J.S., Stone,M.P. and Rizzo,C.J. (2007) Conformational differences of the C8-deoxyguanosine adduct of 2-amino-3-methylimidazo[4,5-f]quinoline (IQ) within the *Nar*I recognition sequence. *Chem. Res. Toxicol.*, **20**, 445–454.

39. Wang,F., DeMuro,N.E., Elmquist,C.E., Stover,J.S., Rizzo,C.J. and Stone,M.P. (2006) Base-displaced intercalated structure of the food mutagen 2-amino-3-methylimidazo[4,5-f]quinoline in the recognition sequence of the *Nar*I restriction enzyme, a hotspot for -2 bp deletions. *J. Am. Chem. Soc.*, **128**, 10085–10095.

40. Wang,F., Elmquist,C.E., Stover,J.S., Rizzo,C.J. and Stone,M.P. (2007) DNA sequence modulates the conformation of the food mutagen 2-amino-3-methylimidazo[4,5-f]quinoline in the recognition sequence of the *Nar*I restriction enzyme. *Biochemistry*, **46**, 8498–8516.

41. Brown,K., Hingerty,B.E., Guenther,E.A., Krishnan,V.V., Broyde,S., Turteltaub,K.W. and Cosman,M. (2001) Solution structure of the 2-amino-1- methyl-6-phenylimidazo[4,5-b]pyridine C8-deoxyguanosine adduct in duplex DNA. *Proc. Natl Acad. Sci. USA*, **98**, 8507–8512.

42. Koehl,P., Valladier,P., Lefevre,J.F. and Fuchs,R.P. (1989) Strong structural effect of the position of a single acetylaminofluorene adduct within a mutation hot spot. *Nucleic Acids Res.*, **17**, 9531–9541.

43. Veaute,X. and Fuchs,R.P. (1991) Polymorphism in N-2-acetylaminofluorene induced DNA structure as revealed by DNase I footprinting. *Nucleic Acids Res.*, **19**, 5603–5606.

44. Gillet,L.C., Alzeer,J. and Scharer,O.D. (2005) Site-specific incorporation of N-(deoxyguanosin-8-yl)-2-acetylaminofluorene (dG-AAF) into oligonucleotides using modified 'ultra-mild' DNA synthesis. *Nucleic Acids Res.*, **33**, 1961–1969.

45. Shapiro,R., Hingerty,B.E. and Broyde,S. (1989) Minor-groove binding models for acetylaminofluorene modified DNA. *J. Biomol. Struct. Dyn.*, **7**, 493–513.

46. Zou,Y., Luo,C. and Geacintov,N.E. (2001) Hierarchy of DNA damage recognition in Escherichia coli nucleotide excision repair. *Biochemistry*, **40**, 2923–2931.

47. Malta,E., Verhagen,C.P., Moolenaar,G.F., Filippov,D.V., van der Marel,G.A. and Goosen,N. (2008) Functions of base flipping in E. coli nucleotide excision repair. *DNA Repair*, **7**, 1647–1658.

48. Malta,E., Moolenaar,G.F. and Goosen,N. (2006) Base flipping in nucleotide excision repair. *J. Biol. Chem.*, **281**, 2184–2194.

49. Scharer,O.D. (2011) Multistep damage recognition, pathway coordination and connections to transcription, damage signaling, chromatin structure, cancer and aging: current perspectives on the nucleotide excision repair pathway. *DNA Repair*, **10**, 667.

50. Liu,Y., Reeves,D., Kropachev,K., Cai,Y., Ding,S., Kolbanovskiy,M., Kolbanovskiy,A., Bolton,J.L., Broyde,S., Van Houten,B. *et al.* (2011) Probing for DNA damage with beta-hairpins: similarities in incision efficiencies of bulky DNA adducts by prokaryotic and human nucleotide excision repair systems in vitro. *DNA Repair*, **10**, 684–696.

51. Ruan,Q., Liu,T., Kolbanovskiy,A., Liu,Y., Ren,J., Skorvaga,M., Zou,Y., Lader,J., Malkani,B., Amin,S. *et al.* (2007) Sequence context- and temperature-dependent nucleotide excision repair of a benzo[a]pyrene diol epoxide-guanine DNA adduct catalyzed by thermophilic UvrABC proteins. *Biochemistry*, **46**, 7006–7015.